UKAEA-CCFE-CP(21)05

C J Ham, A Bokshi, D Brunetti, G Bustos Ramirez, B Chapman, J W Connor, D Dickinson, A R Field, J P Graves, T Kiviniemi, S Leerink, B McMillan, S Newton, S Pamela, C M Roach, S Saarelma, J Simpson, S F Smith, P Strand, A Virtanen, the JET Contributors*

Understanding reactor relevant tokamak pedestals

Understanding reactor relevant tokamak pedestals

C J Ham, A Bokshi, D Brunetti, G Bustos Ramirez, B Chapman, J W Connor, D Dickinson, A R Field, J P Graves, T Kiviniemi, S Leerink, B McMillan, S Newton, S Pamela, C M Roach, S Saarelma, J Simpson, S F Smith, P Strand, A Virtanen, the JET Contributors*

This paper has been submitted to
28th IAEA Fusion Energy Conference, Nice, France, 10-15th May 2021

Understanding reactor relevant tokamak pedestals

C J Ham[1], A Bokshi[2], D Brunetti[1], G Bustos Ramirez[3], B Chapman[1], J W Connor[1], D Dickinson[4], A R Field[1], L Frassinetti[5], A Gillgren[9], J P Graves[3], T P Kiviniemi[6], S Leerink[6], B McMillan[7], S Newton[1], S Pamela[1], C M Roach[1], S Saarelma[1], J Simpson[1], S F Smith[1], E R Solano[8], P Strand[9], A J Virtanen[6] and the JET Contributors*

[1]UKAEA-CCFE, Culham Science Centre, Abingdon, Oxon, OX14 3DB, UK.[2]Institute for Plasma Research, Gandhinagar, India; [3]EPFL, Swiss Plasma Center, CH-1015 Lausanne, Switzerland; [4]York Plasma Institute, University of York, Heslington, York YO10 5DD, UK; [5]Division of Fusion Plasma Physics, KTH, Stockholm SE; [6]Aalto University, FI-00076 Aalto, Finland; [7]University of Warwick, Coventry CV4 7AL, UK; [8]Laboratorio Nacional de Fusin, CIEMAT, Madrid, Spain; [9]Chalmers University of Technology, SE-412 96 Gothenburg, Sweden; *See author list of E. Joffrin et al., Nucl. Fusion 59 112021 (2019)

E-mail: `christopher.ham@ukaea.uk`

Abstract. The physics of the tokamak pedestal is still not fully understood. However, this will be a key element for improving our confidence in designing potential fusion power plants. There is no fully predictive model for the pedestal height and width for example. Work has been carried out as part of a collaboration on reactor relevant pedestal physics. We report here some of the results and also review some of the wider work which will be reported in full elsewhere. First, we attempt to use a gyrokinetic-based calculation to eliminate the pedestal top density as a model input for Europed/EPED pedestal predictions. We assume power balance at the top of the pedestal, that is, the heat flux crossing the separatrix must be equal to the heat source at the top of the pedestal and investigate the consequences of this assumption. Unfortunately, this method was not successful. Second, we investigate the effects of non flux surface density on the bootstrap current. Third, type I ELMs will not be tolerable for a reactor relevant regime due to the damage that they are expected to cause to plasma facing components. In recent years various methods of running tokamak plasmas without large ELMs have been developed. These include small and no ELM regimes, the use of resonant magnetic perturbations and the use of vertical kicks. We discuss the quiescent H-mode here. Finally we give directions for future work.

Submitted to: *Plasma Phys. Control. Fusion*

1. Introduction

1.1. Background

The pedestal, which is associated with a local formation of a transport barrier (in energy and particles), plays an important role in determining the confinement in tokamak H-mode plasmas. Indeed the increased confinement associated with the steep pedestal gradients strongly affect the global plasma performance, and the expected fusion power associated with a given scenario. However, the steep pressure gradients in this transport barrier also lead to edge localized modes (ELMs) [1]. There is a reasonable understanding of the pedestal in type I ELM regimes being limited by ideal MHD peeling-ballooning modes. The EPED model can predict pedestal height and width of type I ELMing plasmas on current machines given various assumptions [2], however, type I ELMs are known to damage plasma facing components and so future large tokamaks must operate with small or no ELMs. Our collaboration aimed to understand various aspects of the physics of reactor relevant pedestals. We document some of the new results here and review the work that will appear in detail elsewhere. There is still much to understand and we will give our thoughts on where future efforts could be directed.

1.2. Overview

In Section 2 we review recent work, especially that carried out as part of our collaboration, which improves our understanding of pedestal physics which is relevant to reactors. In Section 3 we describe the work we have done on improving pedestal prediction models. In particular, making the EUROPED model [3] more general and building our understanding of the physics that underlies the model. In Section 4 we investigate how a non flux surface density, i.e. density is not constant on a flux surface, may change the bootstrap current. In Section 5 we discuss the improvements we have made in our understanding of the QH mode. We finish with a summary and directions for future work in Section 6.

2. Recent work on Reactor Relevant Pedestals

The pedestal continues to be a rich source of interesting physics and we still do not have a solid understanding of the underlying processes. It is important that we develop our understanding of the pedestal not just because of the interesting physics but also because to design and build future tokamak fusion reactors we must be able to predict pedestals to give confidence that potential designs will operate at the required performanace.

The EPED and EUROPED models have had some success in this area but they have underlying assumptions that to one degree or another are based on experimental observations. One such assumption is the pedestal gradient being limited by the $\sqrt{\beta_{pol}}$. This is an assumption about the transport and the instabilities that are assumed to produce that transport. We report work in Section 3 that seeks to improve our approach in this area.

A further important part of the physics of the pedestal is the bootstrap current that is generated by the steep pressure gradient in the pedestal region. There are various ways of calculating the bootstrap current that involve either direct solution of the neoclassical equations [4, 5] or a fitting of the numerical solution over various parameter ranges [6], [7]. Members of our collaboration have used the global full f gyrokinetic code ELMFIRE [8] first to benchmark the Hager and Sauter models [9]. It was found that these two formulae agree with ELMFIRE in the regime where there is no Shafranov Shift and low collisionality, which is relevant for ELMFIRE. Further, ELMFIRE has been used to assess the effect of poloidal variation of density on the bootstrap current [9]. Initial results indicate that there is an effect which should be investigated further. Analytic calculations of the effect of poloidal variation of density have been carried out and this analysis is presented in Section 4. We have also investigated the effect of poloidal variation of density on MHD stability using the JOREK code [10]. The initial results showed that the growth rate of low toroidal mode number instabilities were affected but further work is required to confirm this.

Integrating all of the pedestal models together and running them could be quite time consuming if the pedestal prediction is part of a design loop for a reactor design or to design a shot or indeed to interpret experimental results. Members of our collaboration have therefore been investigating the use of neural networks. These neural networks can be trained either on experimental data or on the results of modelling and the resulting neural network can then be used to produce fast pedestal predictions. This has been completed for JET using PENN [11].

Our collaboration investigated some of the small and no ELM regimes that will have to be considered for a reactor. The quiessent H-mode (QH-mode) is one such ELM free regime that has been investigated in DIII-D [12], JET [13] and at AUG [14]. The plasma still has a pedestal and so has reactor relevant performance but it develops an edge harmonic oscillation (EHO) which is thought to be a saturated MHD mode. This is thought to produce sufficient density transport such that the peeling ballooning (PB) mode boundary is not reached and so the ELM is avoided. Experimental evidence so far suggests that an edge rotation shear is required for the QH-mode to appear. Our collaboration has investigated the QH-mode both numerically and analytically. We have used the VMEC code to find saturated nonlinear MHD states [15]. These can be found in two regimes. One where the safety factor profile (q profile) is just below a rational at the plasma edge. This is the classical external kink mode. The other is a pressure driven mode that requires a flattening of the q profile at the edge. This flattening is provided by the bootstrap current which is driven by the pressure gradient in the pedestal. The ballooning stability of these two saturated instabilities is discussed in Section 5. The QH-mode in JET has also been investigated and in particular the effect of collisionality [16]. A model for Grassy ELMs has been investigated using a gyrofluid model implimented in the BOUT++ framework. Initial tests of the model have been completed but further work will be required to test it in the appropriate regime. An analytic model of type III ELMs has been developed based on a resistive MHD model and this will be discussed elsewhere [17].

3. Pedestal Prediction

In this Section we seek to improve the well known EPED model. This model has various assumptions underlying it. In particular, one input is the density at the pedestal top. We aim here to use a gyrokinetic-based calculation to eliminate this input. This idea is to assume power balance at the top of the pedestal, that is, the heat flux crossing the separatrix must be equal to the heat source at the top of the pedestal. The workflow is as follows: use Europed with a range of $n_{e,ped}$ as input to get a corresponding range of $T_{e,ped}$; use a gyrokinetic-based calculation to test each pair of profiles and calculate the heat flux Q_{ped} and; then the pedestal prediction is the n_e, T_e profile pair with Q_{ped} equal to the experimental heat flux.

A key part is to calculate the heat flux. There are a number of options available which include: full, multi-scale gyrokinetic simulations including neoclassical terms; a trio of gyrokinetic simulations: nonlinear global ion-scale, nonlinear local electron-scale, neoclassical; quasilinear model with linear gyrokinetic simulations; quasilinear model with eigensolver e.g. QuaLiKiz [18] and finally; fast Neural network-type software trained on any of the above.

Work is underway to develop a sophisticated quasilinear model in the pedestal. At the time of writing a comprehensive quasilinear model that can be used reliably and routinely has not been published. To match the heat flux we must therefore run fully non-linear simulations that capture the spatial and temporal scales of the turbulence believed to be the primary source of heat flux through the pedestal. However, the computational expense of such simulations is prohibitive. We therefore opt for a comparison to linear spectra instead. As we shall see, it is unlikely that further information would be obtained from nonlinear simulations.

In order to test the heat flux matching concept we examine JET-ILW pulse #84793 which lies along the peeling-ballooning stability boundary, Fig. 1 [19], and therefore satisfies one of the key EPED model assumptions. We start by assuming slab-ETG modes are the primary driver of turbulent heat flux, and neglect neoclassical heat flux, which can easily be added to the model later. We use the GENE gyrokinetic code [20, 21] in its local model of operation. The resolution requirements for this pulse are known from previous analysis. Before continuing, it is first necessary to test the validity of the EPED model and discuss some of the features and extensions of Europed that are required in order to fulfil our objective.

3.1. Europed results

3.1.1. Details of the EPED model and Europed package The two principle assumptions of the EPED1 model are: a) an ideal-MHD constraint - the pedestal is limited by Peeling-Ballooning modes, and b) a transport constraint - the width of the pressure pedestal scales with the square-root of the pedestal poloidal beta according to: $\Delta_p = C\beta_{p,ped}^{1/2}$; where C is a model constant. The two main inputs to the EPED model are the global beta β_N or β_p, and the value of density at the pedestal top $n_{e,ped}$. In addition, the standard EPED1 model has the following fixed assumptions: $\Delta_p = \Delta_{T_e} = \Delta_{n_e}$; the density and temperature profiles are aligned to the same pedestal position; the profiles are well described by a mtanh fit; and $T_i = T_e$.

EPED1 also has three notable variable assumptions which are usually device specific: the transport constraint model constant $C = 0.076$; $T_{e,sep} = 100$eV for JET-ILW [22, 23] and; $n_{e,sep} = f \times n_{e,ped}$ where f is a constant - we often use $f = 0.25$.

The value of the model constant C can be obtained from an empirical fit to experimental

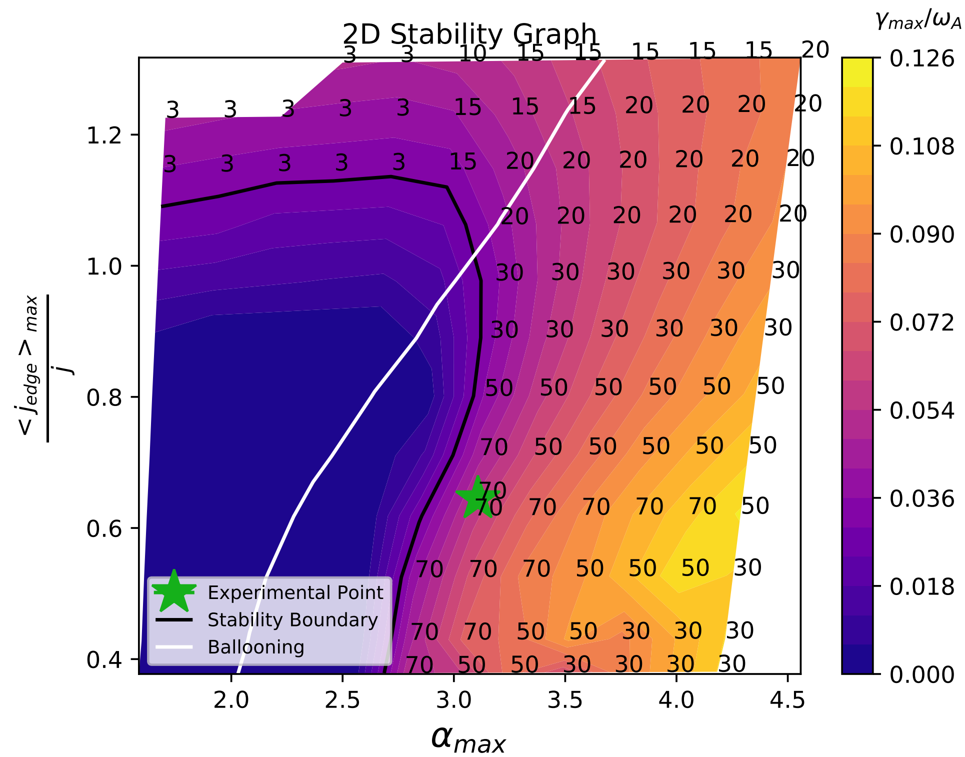

Figure 1. Linear MHD pedestal stability analysis for the deuterium plasma #84793, $I_p = 1.4MA, B_t = 1.7T$. The numbers indicate the most unstable mode number at given edge current and pressure gradient.

data. The value of $T_{e,sep}$ is device specific but in the case of JET-ILW, this is borne out well by edge modelling. The relationship $n_{e,sep}/n_{e,ped} = 1/4$ is less well-founded, but the pressure profile prediction from EPED1 appears to be relatively insensitive to this. As we shall see later, the choice of $n_{e,sep}$ may have important consequences for the stability of slab-like microinstabilities in the pedestal. In practice, the density peaking factor, related to the core density, must also be specified. However, pedestal predictions are mostly insensitive to this so we omit it from discussion here. The Europed package consists of the EPED series of models along with some additional functionality. Chief among these are several models for the self-consistent heating in the core which allow for an arbitrary core profile shape; and two models which allow us to specify $n_{e,ped}$ [24]. These models are not the subject of this work and we will be running Europed in the beta constrained mode of operation with $n_{e,ped}$ specified according to our model. There are two extensions of the EPED model within Europed that are critical for the heat flux matching concept discussed in the following. The first is the ability to specify a relative shift, δ_{n-T}, between the density and temperature pedestals, an important feature of JET-ILW pedestals [23]. The second is the possibility of specifying the ratio $\Delta_{T_e}/\Delta_{n_e}$, which was implemented as part of this project.

3.1.2. Europed runs - the effect of $\Delta_{T_e} \neq \Delta_{n_e}$ and $\delta_{n-T} \neq 0$ It is well known that an important parameter related to the linear stability of slab-ETG modes is the ratio of the normalised density and temperature scale lengths η_e given by:

$$\eta_e = \frac{dln(T_e)}{dln(n_e)} = \frac{n_e \nabla T_e}{T_e \nabla n_e} = \frac{1/L_{T_e}}{1/L_{n_e}} = \frac{L_{n_e}}{L_{T_e}}. \tag{1}$$

Previous work by F. Jenko and others has shown that strong linear slab-ETG drive requires $\eta_e \gtrsim 1$ [20]. The standard EPED assumptions that the temperature and density pedestal positions, henceforth referred to as $\Psi_{N,Te}$ and $\Psi_{N,ne}$ respectively, are aligned, and the pedestal widths Δ_{T_e} and Δ_{n_e} are equal, mean that $\eta_e \approx 1$ across the pedestal region by design. To this end, we explore the consequences of a finite relative shift $\delta_{n-T} = \Psi_{N,ne} - \Psi_{N,Te} \neq 0$ and $\Delta_{T_e} \neq \Delta_{n_e}$ on Europed predictions for JET-ILW pulse #84793. Figure 2 shows the experimental profiles in dotted black along with the results of four Europed runs. Dashed lines correspond to $\delta_{n-T} = 0$ whereas solid lines correspond to $\delta_{n-T} = 0.8\%$. Blue lines denote the default EPED assumption $\Delta_{T_e}/\Delta_{n_e} = 1$ while red lines show the results in which $\Delta_{T_e}/\Delta_{n_e} = 1.76$ (chosen to match experiment), made possible by newly implemented functionality. Note that a corollary of the latter input is that $\Delta_{n_e} < \Delta_{p_e} < \Delta_{T_e}$ [25]

In all four cases, the predicted Δ_p varied between ~ 0.030 and 0.034, i.e. Δ_p is relatively insensitive to these modifications between the relationship between the density and temperature pedestals. We also note in passing that the Europed predicted Δ_p is approximately equal to the experimental Δ_{n_e}, a feature that will be explored in future work with a larger experimental dataset. In these four runs we set $n_{e,sep} = 0.33 n_{e,ped}$, which, in the case of a finite relative shift and equal density and temperature pedestal widths, matches the experiment almost exactly. This is because of the aforementioned, and perhaps coincidental, correspondence between the Europed predicted Δ_{n_e} and the experimental Δ_p. The solid traces show that, in general, δ_{n-T} influences pedestal profile prediction more than having $\Delta_{T_e} \neq \Delta_{n_e}$. The solid red line has the most physical effects in that δ_{n-T} and $\Delta_{T_e}/\Delta_{n_e}$ have been chosen to match experiment. This prediction therefore gives the closest match in $T_{e,ped}$ to experiment, but under-predicts the width of both the density and temperature pedestals. Note that this prediction required the input of two known quantities from experiment. Figure 3 displays: η_e, the normalised density gradient, and the normalised temperature gradient corresponding to the profiles shown in Fig. 2. The colour scheme and line-styles are the same as Fig. 2. The dashed blue line, corresponding to the standard EPED1 prediction, shows identical density and temperature gradients in the steep gradient region, along with a flat $\eta_e \sim 1$ trace. Looking at the solid blue line we see that the finite relative shift has flattened the density profile in the pedestal region ($\Psi_N \leq 1$) which results in a larger, and non-constant value of η_e more in line with experiment. In the dashed red line, with no relative shift but unequal pedestal widths, the Δ_{n_e} prediction has decreased which has realised in a normalised density gradient much larger than the experimental value. This has the effect of lowering η_e. However, as $\Delta_{T_e}/\Delta_{n_e} > 1$ means $\Delta_{T_e} > \Delta_p$, the normalised temperature gradient is less than that of the standard EPED1 prediction (dashed blue trace). These two effects, larger density gradient

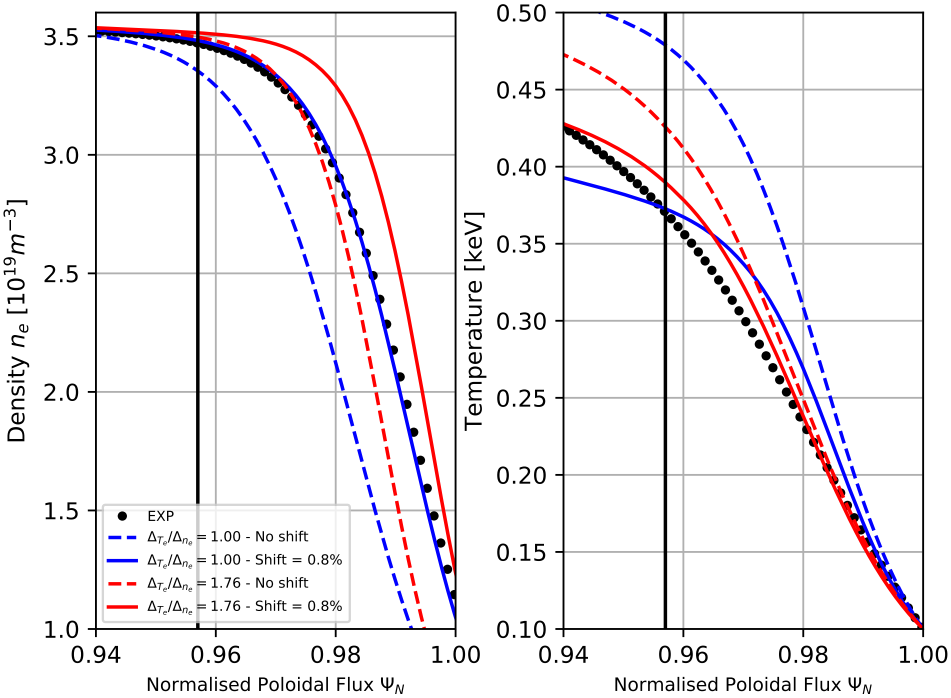

Figure 2. Density (left) and electron temperature (right) as a function of normalised Ψ_N in the pedestal region for JET-ILW pulse #84793. An mtanh fit to raw HRTS data is shown in black. Blue traces show Europed predictions with $\Delta_{T_e}/\Delta_{n_e} = 1.0$ (the default EPED assumption), while red traces show Europed predictions with $\Delta_{T_e}/\Delta_{n_e} = 1.76$ (the experimental value). Dashed traces show Europed predictions with $\delta_{n-T} = 0$ (the default EPED assumption), while red traces show Europed predictions with $\delta_{n-T} = 0.8\%$ (the experimental value). In both panels, the vertical black line denotes $\Psi_N \approx 0.956$, which is the location of the temperature pedestal top for the widest pedestal prediction. Europed data points with $\Psi_N \lesssim 0.956$ are therefore outside the range of accurate Europed predictions.

and smaller temperature gradient, compensate for each other and lead to an η_e profile which closely resembles the experimental profile. When we add a relative shift to this, shown in the solid red trace, the flat density profile increases η_e to larger values than experiment. Thus, despite having less physical effects, the dashed red trace seems to be a better predictor of η_e than the solid red trace. This is a coincidence, the normalised density gradient profile is clearly not in line with experiment.

3.2. Proof-of-principle test

We now proceed to test our heat flux matching idea for this pulse using our proxy method of comparing the linear spectra. Recall that the aim is to eliminate $n_{e,ped}$ as an input variable in the EPED model. Using the experimental values of $\delta_{n-T} = 0.8\%$ and $\Delta_{T_e}/\Delta_{n_e} = 1.76$, we perform a three point scan of $n_{e,ped}$ centred on the experimental value using: $3.0 \times 10^{19} m^{-3}$, $3.5 \times 10^{19} m^{-3}$, and $4.0 \times 10^{19} m^{-3}$. We again set $n_{e,sep} = 0.33 n_{e,ped}$. We have modified

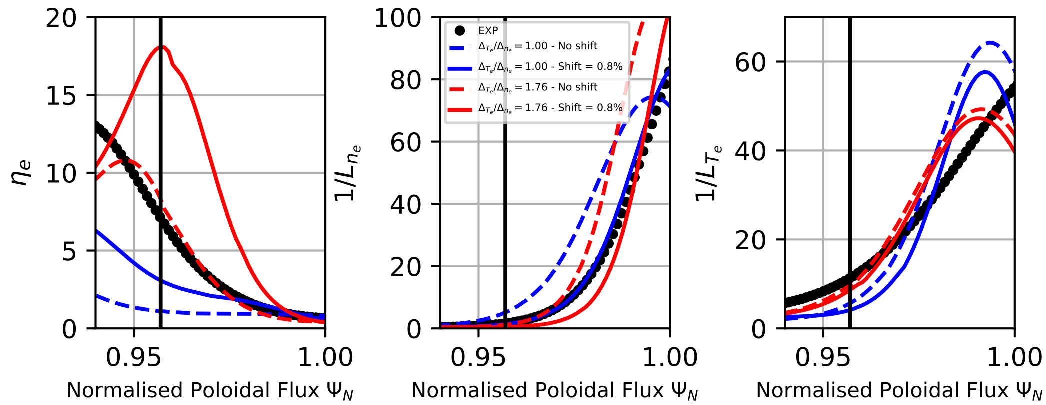

Figure 3. η_e (left), normalised density gradient (middle), and normalised temperature gradient (right) as a function of normalised Ψ_N in the pedestal region for JET-ILW pulse #84793. Experimental data is shown in black. Blue traces show Europed predictions with $\Delta_{T_e}/\Delta_{n_e} = 1.0$ (the default EPED assumption), while red traces show Europed predictions with $\Delta_{T_e}/\Delta_{n_e} = 1.76$ (the experimental value). Dashed traces show Europed predictions with $\delta_{n-T} = 0$ (the default EPED assumption), while red traces show Europed predictions with $\delta_{n-T} = 0.8\%$ (the experimental value). In both panels, the vertical black line denotes $\Psi_N \approx 0.956$, which is the location of the temperature pedestal top for the widest pedestal prediction. Europed data points with $\Psi_N \lesssim 0.956$ are therefore outside the range of accurate Europed predictions.

Europed so that once the pedestal profile has been predicted, the code runs an instance of HELENA followed by CHEASE to produce an eqdsk equilibrium file for use in GENE simulation for the prediction. The profiles that result from this scan are shown in Fig. 4 and a plot of η_e and the normalised gradients are shown in Fig. 5. We immediately see from the left panel of Fig. 4 that that Δ_{n_e} turns out to be approximately the same in all three cases. This is because the Europed Δ_p prediction is approximately the same, and the two widths are related to each other by a constant scale factor. A consequence of this is that $\beta_{p,ped} \propto \Delta_p^2$ is approximately constant, which in turn means that as $n_{e,ped}$ increases, $T_{e,ped}$ decreases in a predictable fashion according to $\propto 1/n_{e,ped}$. As expected, the scan point closest to the experimental value (orange) predicts pedestals that are closest experiment (black).

Looking at the centre panel of Fig. 5, we see that the normalised density gradients are very-nearly the same for the three scan-points (they are minutely different due to differences in $n_{e,sep}$). This is because the Δ_{n_e} prediction is the same for all three runs and the un-normalised density gradient scales with the input $n_{e,ped}$. We also see that the normalised temperature gradients are of similar value across a wide range of the pedestal. The values of $1/L_{T_e}$ do change towards the separatrix, but this is a consequence of fixing $T_{e,sep} = 100$eV for differing values of $T_{e,ped}$. The combined effect of these two things is that the η_e profiles in the pedestal region (to the right of the vertical black line) are indistinguishable.

Given the similarity of the η_e, a/L_{n_e}, and a/L_{T_e} profiles, we expect no substantial difference in the linear spectra and nonlinear flux for the three scanpoints. There may be some difference in the GENE spectra for simulations at $\Psi_N \sim 0.98$ if the excited modes are driven primarily by changes in a/L_{T_e}. As discussed, the changes in the a/L_{T_e} profiles $\Psi_N \sim 0.98$ are a

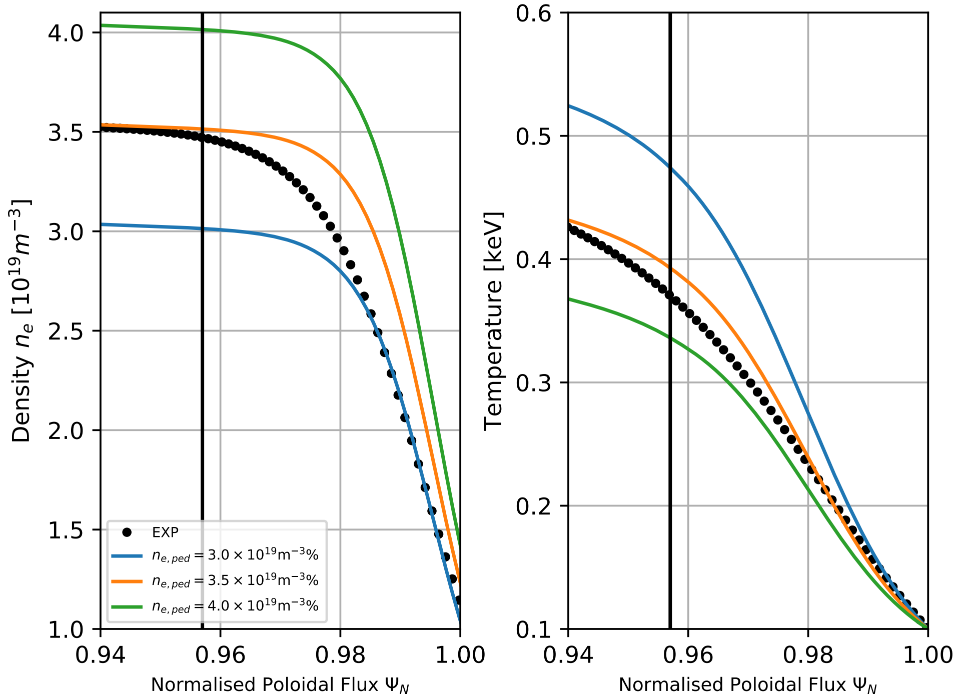

Figure 4. Density (left) and electron temperature (right) as a function of normalised Ψ_N in the pedestal region for JET-ILW pulse #84793. An mtanh fit to raw HRTS data is shown in black. Blue, orange, and green traces show Europed pedestal predictions using $3.0 \times 10^{19} m^{-3}$, $3.5 \times 10^{19} m^{-3}$, and $4.0 \times 10^{19} m^{-3}$ respectively. In both panels, the vertical black line denotes $\Psi_N \approx 0.956$, which is the location of the temperature pedestal top for the widest pedestal prediction. Europed data points with $\Psi_N \lesssim 0.956$ are therefore outside the range of accurate Europed predictions.

consequence of fixing $T_{e,sep} = 100$eV. For the moment, we assume this change in the a/L_{T_e} profile has physical meaning and proceed to run a trio of linear local GENE simulations at $\rho_t = 0.98$ (in the vicinity of $\Psi_N \sim 0.98$). The resolution requirements for these simulations is known from previous work, and we restrict our attention to modes at the outboard mid-plane, that is $\theta_0 = 0$. Figure 6 shows the linear normalised growth rate γ as a function of the binormal wavenumber k_y. The red trace shows the equivalent calculation using the experimental profiles for this pulse. The modes present in the experimental profiles have a smaller peak γ than the spectra produced using the Europed predicted profiles predictions. More importantly, the growth rate spectra for the three Europed profile predictions are extremely similar. We emphasise that even these small variations in the spectra are almost entirely a consequence of fixing $T_{e,sep} = 100$eV. Past experience suggests that the nonlinear counterparts of linear simulations with extremely similar spectra will also predict extremely similar heat fluxes. We conclude that for this pulse, and this range of scanpoints, it is not possible to use gyrokinetic simulations as a means of eliminating $n_{e,ped}$ as an input variable.

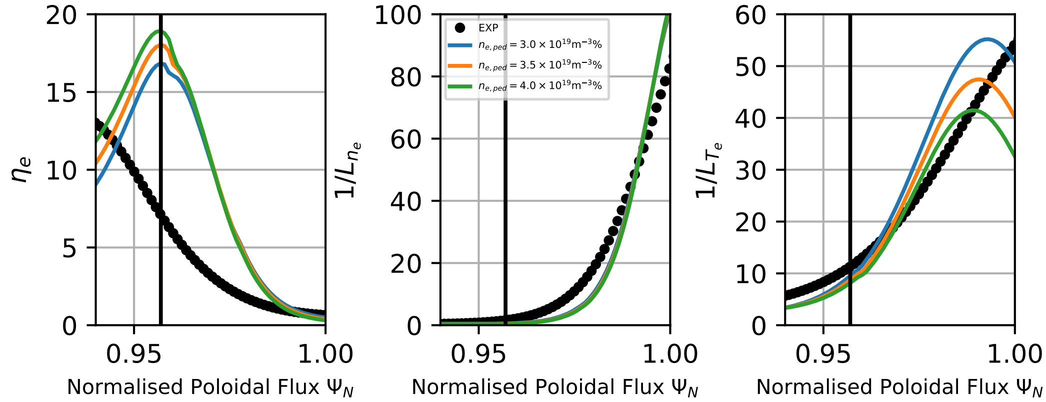

Figure 5. η_e (left), normalised density gradient (middle), and normalised temperature gradient (right) as a function of normalised Ψ_N in the pedestal region for JET-ILW pulse #84793. Experimental data is shown in black. Blue, orange, and green traces show Europed predictions using $3.0 \times 10^{19} m^{-3}$, $3.5 \times 10^{19} m^{-3}$, and $4.0 \times 10^{19} m^{-3}$ respectively. In both panels, the vertical black line denotes $\Psi_N \approx 0.956$, which is the location of the temperature pedestal top for the widest pedestal prediction. Europed data points with $\Psi_N \lesssim 0.956$ are therefore outside the range of accurate Europed predictions.

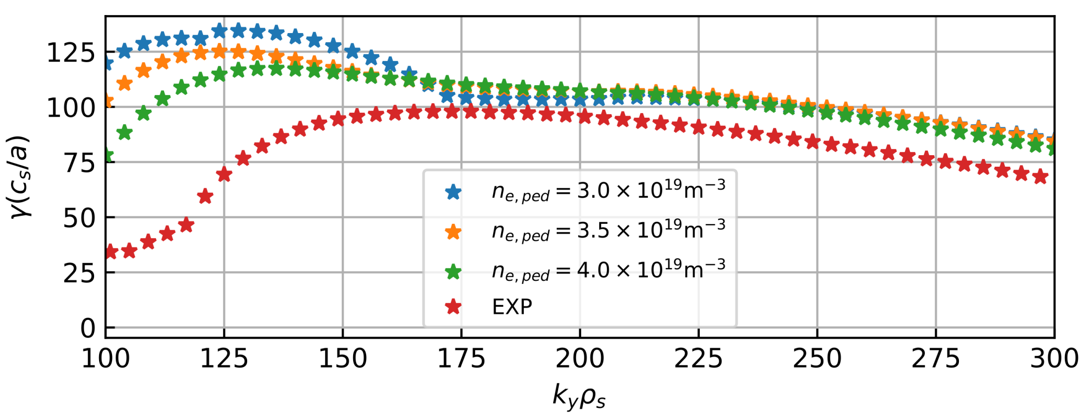

Figure 6. Growth rates as a function of binormal wavenumber k_y of slab-ETG modes from linear local GENE simulations at $\rho_t = 0.98$ for JET-ILW pulse #84793. The red trace corresponds to the experimental profiles at the same flux surface. Blue, orange, and green traces show Europed pedestal predictions using $3.0 \times 10^{19} m^{-3}$, $3.5 \times 10^{19} m^{-3}$, and $4.0 \times 10^{19} m^{-3}$ respectively.

3.3. Discussion

In this work we have tested the feasibility of using a gyrokinetic-based calculation as a means of eliminating the pedestal top density $n_{e,ped}$ as an input into the EPED/Europed model. Using a JET-ILW pulse lying along the Peeling-Ballooning boundary as our test case, we found that in order for the Europed predictions to approach experiment the effects of relative shift $\delta_{n-T} = \Psi_{N,ne} - \Psi_{N,Te}$ and non-equal temperature and density pedestal widths had to be included. We found that this was necessary in order to predict T_e and n_e profiles that have $\eta_e > 1$ and are hence susceptible to slab-ETG instabilities, which have been found to be important [26, 27]. In addition, we upgraded Europed to allow for $\Delta_{T_e}/\Delta_{n_e} \neq 1$ and to produce equilibrium files for use in gyrokinetic simulations. Note that these features allow us to predict profiles susceptible to slab-ITG instabilities as the EPED assumption $T_i = T_e$ results in $\eta_i = \eta_e$.

These additional physical effects aside, we found that for a range of $n_{e,ped}$ around the experimental value, the Europed predicted profiles were too similar for a linear gyrokinetic calculation to accurately distinguish between input profiles. We fully expect this result to carry over to a nonlinear calculation of heat flux, meaning it is currently not possible to use gyrokinetic simulations as a means of eliminating $n_{e,ped}$ as an input variable. The source of this limitation may lie within the EPED transport constraint $\Delta_p = C\beta_{p,ped}^{1/2}$. This relationship means that for a given shot, the predicted Δ_p and $\beta_{p,ped}$ will always be similar over a wide range of inputs. In evidence, a scan of δ_{n-T} from 0.4% to 1.1% (not shown here) resulted in a variation in the predicted Δ_p changes by only $\sim 9\%$. In the results discussed in previous sections, changing $\Delta_{T_e}/\Delta_{n_e}$ changed Δ_p by $\sim 4\%$ for $\delta_{n-T} = 0$ and by $\sim 13\%$ for $\delta_{n-T} = 0.8\%$. Most importantly, for the cursory $n_{e,ped}$ scan discussed above, Δ_p changed by only $\sim 5\%$. These small variations in $\Delta_p^2 \propto \beta_{p,ped} \propto T_{e,ped}$ mean that for an $n_{e,ped}$ scan, the normalised density and temperature gradients will always be similar, which in turn means the value of $\eta_e = \eta_i$ will always be similar.

In conclusion, using a gyrokinetic based calculation to eliminate $n_{e,ped}$ as an EPED/Europed input is not feasible until the transport assumption $\Delta = C\beta_{p,ped}^{1/2}$ is improved [28]. Such an improvement must be the primary focus of future work. Finally, we note that if $n_{e,ped}$ were known in advance, a gyrokinetic-based heat flux matching calculation may prove useful for eliminating the ratio $\Delta_{T_e}/\Delta_{n_e}$ and/or δ_{n-T} as model inputs, as Fig. 3 shows the driving parameters are much more sensitive to this.

4. Effect of a Poloidal Variation of the Plasma Density on the Bootstrap Current

The use of gas puffing and the result of recycling might be expected to introduce a poloidal variation of the plasma density on a flux surface [29] and it is of interest to investigate the impact this has on the bootstrap current [30] in a plasma H-mode edge pedestal, as it could affect the peeling-ballooning mode stability [31] believed to play a role in the triggering of ELMs in tokamak H-mode. Furthermore, toroidal rotation can also generate a variation in density, with it peaking on the outboard side [32].

We first describe the kinetic equation for a large aspect ratio tokamak geometry with a zero order (in a Larmor radius expansion) plasma distribution function that is a Maxwellian having a poloidally varying density, a model that we use to illustrate the calculation. Then we calculate the increment in the bootstrap current, relative to the standard result, that the poloidal variation in the density produces. However, it may well be that in reality the distribution differs from a simple Maxwellian and additional corrections to our simple model for the bootstrap current might emerge, but these would involve a much more complex calculation. A related paper [33] avoided this difficulty by introducing a source (as a δ-function in poloidal angle) in the first order equation, rather than in lowest order as our Maxwellian ansatz implies. We compare the effect of sinusoidal variations in two situations: one up-down symmetric (case (a)), the other symmetric in the inboard-outboard direction (case (b)). In practice, however, edge modelling codes show the variation due to neutral sources crossing the separatrix may be better represented by a more poloidally localised function [34]. We therefore also consider case (c) where we represent this situation by a δ-function (although assuming the localisation exceeds the electron Larmor radius in order to justify the use of the electron drift kinetic equation in calculating the bootstrap current). We show this solution also serves as a Green's function for an arbitrary poloidal variation in density. Furthermore, it allows one to extend the calculation to describe a general, axisymmetric toroidal geometry although we limit this to toroidal equilibria with a small number of trapped particles to justify the use of the pitch-angle scattering collision operator - and also to up-down symmetric ones, for simplicity. The electron and ion temperatures will also respond to a density variation on a flux surface through rapid electron thermal transport along field lines and pressure equalisation on a flux surface on the sound time scale to produce temperature perturbations that equalises the plasma pressure on the surface. We consider the impact of this, as well as that of the density variation, on the incremental bootstrap current. A numerical investigation of this problem has been carried out using ELMFIRE [9]. Previous work on understanding the effect of a poloidal density variation on transport was carried out by Solano and Hazeltine [35]. This work is in the plateau regime rather than the banana regime and the structure of the source is different.

4.1. The model

The distribution function for species j , f_j , satisfies a kinetic equation

$$\frac{\partial f_j}{\partial t} + \frac{Iv_\parallel}{BR^2 q}\frac{\partial f_j}{\partial \theta} - v_{dj}\cdot\nabla f_j + C_j(f_j) + S(r,\theta,v) = 0 \tag{2}$$

where spatial derivatives are at constant energy. In first order we introduce a source $S(r,\theta,v)$ to ensure a steady state if the drift terms lead to a net flux across a flux surface

Here we use velocity space co-ordinates: v, $\lambda = v_\perp^2/Bv^2$, $\sigma = v_\parallel/|v_\parallel|$, $v_\parallel = \sigma v\sqrt{(1-\lambda B)}$ so that $\int d^3v = \pi\Sigma_\sigma \int Bd\lambda \int v^2 dv/|\sqrt{(1-\lambda B)}$, $v_{dj} = (v_\parallel/B)\times\nabla(v_\parallel/\omega_{cj})$. Specialising to a large aspect ratio tokamak geometry and a steady state situation for simplicity (we indicate how to generalise our results to an arbitrary axisymmetric toroidal geometry later), this can be written [36]

$$\frac{v_\parallel}{Rq}\frac{\partial f_j}{\partial \theta} - \frac{m_j}{e_j}v_\parallel\left(\frac{\partial}{\partial r}\left(\frac{v_\parallel}{B}\right)\frac{\partial f_j}{r\partial\theta} - \frac{\partial}{r\partial\theta}\left(\frac{v_\parallel}{B}\right)\frac{\partial f_j}{\partial r}\right) + C_j(f_j) + S(r,\theta,v) = 0, \tag{3}$$

with $B = B_0(1-\frac{r}{R}\cos\theta)$, so that $\frac{\partial}{\partial r}(v_\parallel/B) = -\frac{\cos\theta}{R}$ and $\frac{\partial}{\partial\theta}(v_\parallel/B) = \frac{\sin\theta}{R}$. We expand $f_j = F_{Mj} + f_{j1}$, where $F_{Mj}(v,r,\theta)$ is the Maxwellian and consider the incremental changes to f_j due to the effects of the perturbations, $\delta n_j(r,)$ and $\delta T_j(r,)$ in F_{Mj}.

To illustrate the calculational formalism, we just consider the effect of a density perturbation: $\delta n_j(r,\theta) = n_{0j}(r)\gamma_j(r)h_j(\theta)$, and assume a Lorentz collision model for the electrons [37]:

$$C_e(f_e) = \nu_{ei}\frac{v_\parallel}{v_{the}^2}\frac{\partial}{\partial\lambda}\left(\frac{v_\parallel\lambda}{B}\frac{\partial}{\partial\lambda}f_e\right) + \nu_{ei}\frac{v_\parallel u_{\parallel i}}{v_{the}^2}F_{Me}, \tag{4}$$

with $u_{\parallel i}$ the mean ion parallel flow. Since we ignore temperature gradients for the moment, the ion distribution is merely a displaced Maxwellian. To capture the effect of the $\delta T_j(r,\theta)$, it will be necessary to include an ion flow, like-particle collisions and the effects of the energy dependence of the collision frequencies [37]; including the former is discussed below and the others later. For the electron density variation, we take

$$n_e(r,\theta) = n_0(r)(1+\gamma(r)h(\theta)). \tag{5}$$

Since we consider the pedestal region, we can also take $\frac{\partial n_e}{\partial r} \gg \frac{1}{r}\frac{\partial n_e}{\partial\theta}$. With these assumptions the effect of the ion flow in the collision operator is merely to combine with the radial derivative of the electron density, which is taken at constant energy in eqn. (3), replacing it by the combination $\frac{\partial n_e}{\partial r} + \frac{T_i}{T_e}\frac{\partial n_i}{\partial r}$, (where we take the ion charge as $Z=1$, so that quasi-neutrality requires $n_e = n_i$. The radial derivatives are of the actual densities as the electrostatic potential terms cancel between the ion and electron contributions (as in standard neoclassical theory). Thus, we have

$$\frac{v_\parallel}{Rq}\frac{\partial f_e}{\partial\theta} - \frac{m_e}{e}v_\parallel F_{Me}\frac{\partial}{\partial r}(\delta n(r,\theta))\frac{\partial}{r\partial\theta}\left(\frac{v_\parallel}{B}\right) + C_e(f_e) + S(r,\theta,v) = 0 \tag{6}$$

with $\delta n = (1+T_i/T_e)\delta n_e$. We take the source to be poloidally symmetric, in which case

$$S(r,v) = -\frac{m_e}{e}F_{Me}\langle\frac{\partial}{\partial r}(\delta n(r,\theta))\frac{\partial}{r\partial\theta}\left(\frac{v_\parallel}{B}\right)\rangle/\langle\frac{1}{v_\parallel}\rangle. \tag{7}$$

4.2. The Incremental Bootstrap Current, δj_{bs}.

The lowest order solution f^0 is:

$$f^0 = \frac{m_e Rq}{e}F_{Me}\left[\int_{\theta_0}^{\theta} d\theta\frac{\partial}{\partial r}(\delta n(r,\theta))\frac{\partial}{r\partial\theta}\left(\frac{v_\parallel}{B}\right) - \int_{\theta_0}^{\theta}\frac{d\theta}{v_\parallel}\langle\frac{\partial}{\partial r}(\delta n(r,\theta))\frac{\partial}{r\partial\theta}\left(\frac{v_\parallel}{B}\right)\rangle\frac{1}{\langle\frac{1}{v_\parallel}\rangle}\right] + g \tag{8}$$

where $\frac{\partial}{\partial\theta}g = 0$ and the end-point contribution from θ_0 to the integral (θ_0 is to be chosen judiciously to simplify calculations) can be absorbed into g. The function g is then determined from a solubility condition arising in first order in the collisional expansion:

$$\langle\frac{\partial}{\partial\lambda}\left(\frac{v_\parallel\lambda}{B}\frac{\partial}{\partial\lambda}f^0\right)\rangle = 0, \tag{9}$$

where the operator $\langle A\rangle = \oint d\theta A/2\pi$ for passing particles and $\langle A\rangle = \frac{1}{2}\Sigma_\sigma\int_{\theta_1}^{\theta_2} d\theta A/2\pi$, with $v_\parallel(\theta_1) = v_\parallel(\theta_2) = 0$, for trapped particles. This determines $\frac{\partial g}{\partial\lambda}$ and hence $\frac{\partial f^0}{\partial\lambda}$. Now the incremental bootstrap current is given by

$$\delta j_{bs} = -e\frac{\oint d\theta}{2\pi}\int d^3v v_\parallel f^0 = e\pi\langle\Sigma_\sigma\int Bd\lambda\int v_\parallel v^3 dv\lambda\partial f^0/\partial\lambda/|v_\parallel|\rangle. \tag{10}$$

We then obtain

$$\delta j_{bs} = -\frac{3}{8}\frac{(T_e+T_i)}{B_\theta}\frac{d}{dr}(n_0(r)\gamma(r))I, \tag{11}$$

where $I = (I_1+I_2)$ with

$$I_1 = 2v\langle\int Bd\lambda B\lambda\left[\int_{\theta_0}^{\theta} d\theta h(\theta)\frac{\partial}{\partial\theta}\left(\frac{1}{v_\parallel}\right) - \frac{1}{\langle|v_\parallel|\rangle}\langle|v_\parallel|\int_{\theta_0}^{\theta} d\theta h(\theta)\frac{\partial}{\partial\theta}\left(\frac{1}{|v_\parallel|}\right)\rangle\right]\rangle, \tag{12}$$

$$I_2 = -2v\langle\int Bd\lambda B\frac{1}{\langle 1/|v_\parallel|\rangle}\left[\int_{\theta_0}^{\theta} d\theta\frac{1}{|v_\parallel|} - \frac{1}{\langle|v_\parallel|\rangle}\langle|v_\parallel|\int_{\theta_0}^{\theta} d\theta\frac{1}{|v_\parallel|}\rangle\right]\langle h(\theta)\frac{\partial}{\partial\theta}\left(\frac{1}{|v_\parallel|}\right)\rangle\rangle, \tag{13}$$

for passing particles, defined to be independent of v. For trapped particles, $I = I_3$ with

$$I_3 = 2v\langle\int Bd\lambda B\left[\langle\int_{\theta_0}^{\theta} d\theta h(\theta)\frac{\partial}{\partial\theta}\left(\frac{1}{|v_\parallel|}\right) - \int_{\theta_0}^{\theta} d\theta\frac{1}{|v_\parallel|}\frac{1}{\langle\frac{1}{|v_\parallel|}\rangle}\rangle\langle h(\theta)\frac{\partial}{\partial\theta}\left(\frac{1}{|v_\parallel|}\right)\rangle\right]\rangle. \tag{14}$$

We can show that I_2 vanishes automatically, independently of $h(\theta)$. To evaluate the integral I over λ, we introduce

$$k^2 = 2\frac{r}{R}\frac{\lambda B_0}{1-\lambda B_0(1-\frac{r}{R})}; \quad v_\parallel = vu(\theta); \quad u = \sqrt{1-k^2\sin^2(\theta/2)} \tag{15}$$

Although $h(\theta)$ can be quite a general periodic function of θ, we first consider the two explicit cases: case (a), $h(\theta) = \cos\theta$ which is up-down symmetric; and case (b), $h(\theta) = \sin\theta$, which is in-out symmetric.

4.3. Case (a) $h(\theta) = \cos\theta$

We obtain

$$I = \frac{4}{\pi}\sqrt{\frac{2r}{R}}\int_0^1 \frac{k^2}{\left(\frac{2r}{R}+k^2\left(1-\frac{r}{R}\right)\right)^{5/2}}\left[\left(1-\frac{2}{k^2}\right)K(k) - \frac{2}{k^2}E(k) - \frac{\pi^2}{2E(k)}\left(1-\frac{2}{k^2}\right)\right]$$
$$+\frac{4}{\pi}\sqrt{\frac{2r}{R}}\int_0^\infty \frac{k^2}{\left(\frac{2r}{R}+k^2\left(1-\frac{r}{R}\right)\right)^{5/2}}\frac{1}{k}\left[\left(3-\frac{4}{k^2}\right)K(\frac{1}{k}) - 2E\left(\frac{1}{k}\right)\right] \tag{16}$$

where K and E are the complete elliptic integrals of the first and second kind, respectively [38]. One can take the limit $r/R \to 0$ and still obtain a convergent integral.

While the first term requires numerical integration, yielding $-0.086\sqrt{(2r/R)}$, the second can again be calculated analytically using properties of the complete elliptic integrals [39], which yields $-20/9\pi\sqrt{(2r/R)} = -0.707\sqrt{(2r/R)}$. Consequently

$$\delta j_{bs} = 0.42\sqrt{\frac{r}{R}}qR\frac{(T_e+T_i)}{B_0}\frac{d}{dr}\left(n_0(r)\gamma(r)\right). \tag{17}$$

4.4. *Case (b): $h(\theta) = \sin\theta$*

Here $\hat{I}_1$ vanishes exactly. The trapped region contribution also vanishes. Consequently, $j_{bs} = 0$ for case (b). Because $\hat{I}_1$ vanishes for $h(\theta) = \sin\theta$, a corollary is that for a sinusoidal variation of $h(\theta)$ centred on an arbitrary angle, $\theta = \beta$,

$$\delta j_{bs} = 2.54\sqrt{\frac{r}{R}}qR\frac{(T_e+T_i)}{B_0}\frac{d}{dr}\left(n_0(r)\gamma(r)\right)\cos\beta. \tag{18}$$

4.5. *Case (c): $h(\theta) = \delta(\theta-\alpha)$.*

In this case we set $h(\theta) = \delta(\theta-\alpha)$, where α is the poloidal angle of the neutral influx, to calculate the incremental bootstrap current. We can calculate the integral I_1 in eqn. (12) for passing particles without difficulty. (The term arising from the azimuthal drift gives rise to derivatives of the δ-function, but these lie under double integrals and do not pose a problem, yielding a contribution which is in fact smaller than the one arising from the radial drift in the steep pedestal gradient.) However, employing the previous method is problematic for the trapped particle contribution. This is because the deeply trapped particles only respond to a limited range of pitch angles, depending on the angle α. The end-point contribution in the integration by parts in λ that arises from the maximum value of λ , λ_{Max}, which is no longer at $\lambda = \frac{1}{B_{Min}}$, does not vanish it is, in fact, singular, and is cancelled by a corresponding contribution from the integral term. It is therefore more convenient to calculate the contribution to the bootstrap current from trapped particles directly, as a straightforward integration over λ, rather than employing the integration by parts. This approach requires the distribution function g in the trapped region, which is a constant, and was not needed for the integration by parts method. In fact, $g = 0$ in the trapped region, to satisfy continuity at λ_{Max}. Of course, this needs to be accompanied by a boundary contribution evaluated at the trapped-passing boundary, to compensate for the integration by parts over passing particles which it is still convenient to retain. This boundary term dominates the integral one by a factor $1/2\varepsilon$, as can be readily understood physically: while the trapped particle pitch angle integration over k introduces a factor $(2\varepsilon)^{1/2}$, another from the trapped particle current, which involves the banana width, $\sim (2\varepsilon)^{1/2}a$, and the typical trapped particle velocity $v_{\parallel} \sim (2\varepsilon)^{1/2}v_{the}$ as a third. Thus, this contribution can be neglected, leaving to a simpler calculation of just the trapped passing boundary term, $I_b(\alpha)$. We define

$$G(\alpha,k) = \left[E - E\left(\frac{\alpha}{2},k\right)/2\right], \quad 0 < \alpha < \pi, \tag{19}$$

$$G(\alpha,k) = E\left(\pi - \frac{\alpha}{2},k\right)/2, \quad \pi < \alpha < 2, \tag{20}$$

with $E(\alpha/2,k)$ the incomplete elliptic integral of the second kind [38]. Thus

$$I_1(\alpha) = \sqrt{\frac{2r}{R}}\int_0^1 dk\frac{\sin\alpha}{\left(1-k^2\sin^2\left(\frac{\alpha}{2}\right)\right)^{3/2}}\left[1 - \frac{\alpha}{2\pi} - \frac{G(\alpha,k)}{E(k)}\right] \tag{21}$$

$I_1(\alpha)$ is invariant under the substitution $\alpha \to 2\pi - \alpha$, so is symmetric about $\alpha = \pi$ (i.e., it is up-down symmetric, as is to be expected). There is also a contribution from the trapped region

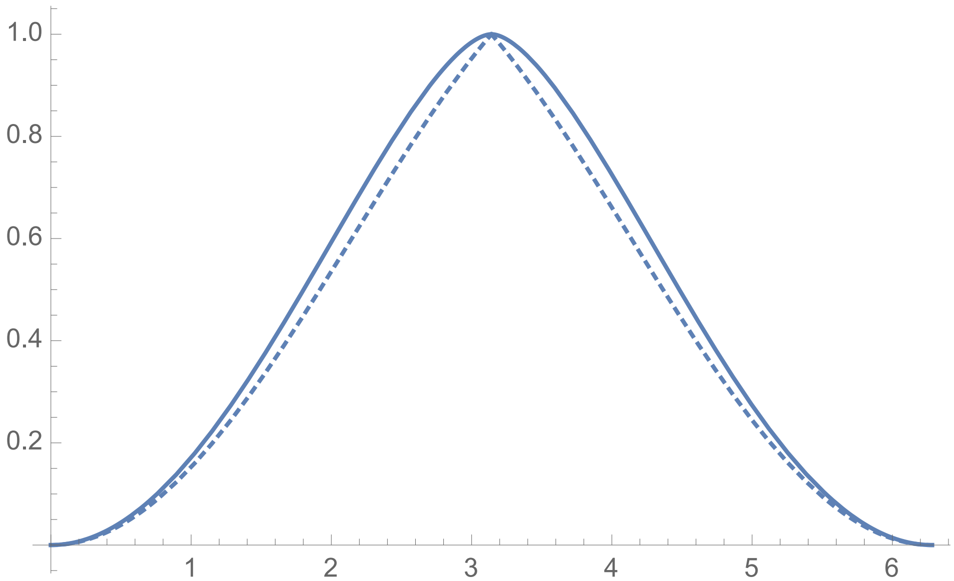

Figure 7. The variation with localisation angle, α, of the integral $\bar{I}(\alpha) = I(\alpha)/\sqrt{2r/R}$ for the δ-function, case (c). The dashed line is the dominant trapped particle contribution

and, as discussed above, this is dominated by the contribution from the flux-surface-averaged, trapped particle current density evaluated at the trapped - passing boundary. Calculating this from f^0 as given by eqn. (8) with $g = 0$, requires the evaluation of

$$I_b(\alpha) = 4\sqrt{\frac{2r}{R}}\langle\int_{\theta_0}^{\theta} d\theta\delta(\theta-\alpha)\frac{\partial}{\partial\theta}(u^{1/2}) - \frac{1}{\langle u^{-1/2}\rangle}\int_{\theta_0}^{\theta} d\theta u^{-1/2}\langle\delta(\theta-\alpha)\frac{\partial}{\partial\theta}(u^{1/2})\rangle\rangle|_{k=1} \tag{22}$$

on the range $-\pi < \alpha < \pi$. this can be evaluated to yield

$$\hat{I}_b(\alpha) = -\frac{1}{2\pi}\sqrt{\frac{2r}{R}}\left[\theta_2 - \alpha - \frac{(\theta_2+\theta_1)}{2}\right] = \frac{1}{\pi}\sqrt{\frac{2r}{R}}\sin(\alpha/2)\alpha, \tag{23}$$

since $\theta_2 = -\theta_1$; this contribution is also symmetric about $\alpha = \pi$, in the range $0 < \alpha < 2\pi$. Therefore, combining the result of a numerical evaluation of eqn. (21) and the analytic expression (23):

$$I(\alpha) = \sqrt{\frac{2r}{R}}\left[\int_0^1 dk\frac{(1-\frac{\alpha}{2\pi}-\frac{G(\alpha,k)}{E(k)})\sin\alpha}{(1-k^2\sin^2(\alpha/2))^{3/2}} + F(\alpha)\right], \tag{24}$$

$$F(\alpha) = \frac{1}{\pi}\alpha\sin(\frac{\alpha}{2}), \quad 0 < \alpha < \pi, \quad F(\alpha) = \frac{1}{\pi}(2\pi-\alpha)\sin(\frac{\alpha}{2}), \quad \pi < \alpha < 2\pi. \tag{25}$$

We notice that this remains finite at $\alpha = \pi$, the bounce point for just trapped particles, although the distribution function f^0 vanishes there; this is because the magnetic drift is singular there and the integration over θ with $h(\theta) = \delta(\theta-\alpha)$ remains finite in the limit $\alpha \to \pi$. (This can be seen more clearly by taking this limit after the integration the integration.)

A plot of $\bar{I}(\alpha) = I(\alpha)/\sqrt{(2r/R)}$ against α is shown in Fig. 7. $I(\alpha)$ vanishes at $\alpha = 0$ and 2π, peaking at $\alpha = \pi$; in between it spans the range $0 < I(\alpha) < \sqrt{(2r/R)}$. Finally, we have

$$\delta j_{bs} = \frac{3}{8}\frac{(T_e + T_i)}{B_\theta}\frac{d}{dr}(n_0(r)\gamma(r))I(\alpha). \tag{26}$$

Although this result is itself significant, the bootstrap current response to the δ-function source also provides a Green's function for a general poloidal density perturbation specified by $\gamma(r)h(\theta)$.

4.6. Green's Function

A consequence of modifying the approach to calculating the bootstrap current that we adopted in the case of the δ-function source was that calculating the trapped particle contribution could be achieved more simply for a general $h(\theta)$ by just considering the trapped particle current density at the trapped-passing boundary, rather than requiring an integration over trapped values of k. Thus, both passing and trapped contributions involve integrations over the full range of θ: $0 < \theta < 2\pi$, rather than the limited range sampled by the trapped particles. This facilitates the demonstration of a Green's function approach based on our solution for the δ-function case, since, as we shall see, the integrations over α and δ that are involved, commute, so one can readily change the orders of these integrations. Thus, we see that the δ-function source provides a Green's function for a poloidal density perturbation specified by $h(\theta) = \delta(\theta - \alpha)$, where we utilise the replacement

$$h(\theta) \rightarrow \oint d\alpha h(\alpha) \tag{27}$$

in eqns. (12), (13) and (14).

4.7. General axisymmetric, toroidal geometry.

We introduce an axisymmetric toroidal co-ordinate system, ψ, θ, ϕ, where ψ is the poloidal flux, θ is a poloidal angle such that the magnetic field lines are straight, and ϕ is the toroidal angle. The magnetic field is given by

$$B = I(\psi)\nabla\phi + \nabla\phi \times \nabla\psi, \tag{28}$$

We now define the operator $\langle\rangle$ by $\langle A\rangle = \oint R^2 d\theta A/\oint R^2 d\theta$. Because of these relations, the solution for f^0, given in eqn. (8), still pertains, provided we use the new definition for $\langle\rangle$, as does the solution for g. From the current continuity equation $\nabla . j = 0$, it follows that the appropriate object to consider in general geometry is the flux-surface average quantity $\langle\delta j_{bs}/B\rangle$ and we obtain

$$\langle\frac{\delta j_{bs}}{B}\rangle = -\frac{3}{8}\frac{I(T_e + T_i)}{qB_{Max}}\frac{d}{d\psi}(n_0(\psi)\gamma(\psi, \theta))I, \tag{29}$$

We follow a parallel set of steps to those used for the large aspect case to obtain a passing contribution

$$I(\alpha) = 2vB_{Max}\frac{\partial}{\partial\alpha}\left(\frac{1}{|v_{\|}|}\left[\frac{\int_{\alpha}^{2\pi} d\theta R^2}{\oint d\theta R^2} - \frac{\int_{\alpha}^{2\pi} d\theta R^2|v_{\|}|}{\oint d\theta R^2|v_{\|}|}\right].(30)$$

For the trapped contribution we find

$$I(\alpha) = F(\alpha) = 4\frac{B_{Max}}{v}\frac{\partial}{\partial\alpha}(\frac{v_{\|}}{B})|_{\lambda=B_{Max}}\left[\frac{\int_{\alpha}^{2\pi} d\theta R^2}{\oint d\theta R^2}\right], 0 < \alpha < \pi, \tag{31}$$

$$I(\alpha) = F(2\pi-\alpha), \quad \pi < \alpha < 2\pi. \tag{32}$$

In the following section we need to extend the collision model to include electron-electron collisions, but this is only completely justified in the limit of a small number of trapped particles, so the general equilibria discussed above are then constrained to satisfy this condition.

4.8. The effect of a poloidal variation in the temperature

If the perturbed pressure is to vanish on a flux surface as required by MHD equilibrium, then

$$\delta p = (T_e + T_i)\delta n + n_0(\delta T_e + \delta T_i) = 0 \tag{33}$$

assuming quasi-neutrality. We also assume equipartition between ion and electron temperatures,

$$T_i = T_e, \quad \delta T_e = \delta T_i \equiv \delta T, \quad so \quad \delta T = \frac{\delta n}{n_0}T_e. \tag{34}$$

Alternatively, rapid parallel electron thermal transport removes the electron temperature perturbation requiring the ion temperature perturbation to facilitate pressure balance, when

$$\delta T_e = 0; \quad \delta T_i = (T_e + T_i)\frac{\delta n}{n_0} \tag{35}$$

If the plasma density source is sufficient to prevent equalisation of pressure a more complex equilibrium must be considered. The analogous results to those for the large aspect ratio case will be equivalent to those for the usual calculation of the bootstrap current driven by equilibrium gradients across constant density flux surfaces with a Lorentz collision operator, apart from the effect of the geometrical factor I. The same situation will be true if we consider the effects of δT with like-particle collisions and energy-dependent collision frequencies, when we can exploit the corresponding results given in Ref. [37]. These calculations give

$$j_{bs} = -1.46(\frac{r}{R})^{1/2}\frac{n_0 T_e}{B_\theta}\left[\left(1+\frac{T_i}{T_e}\right)\frac{1}{n_0}\frac{dn_e}{dr} + \frac{1}{T_e}\frac{dT_e}{dr} - \frac{0.17}{T_e}\frac{dT_i}{dr}\right] \tag{36}$$

for the Lorentz model and

$$j_{bs} = -1.46(\frac{r}{R})^{1/2}\frac{n_0 T_e}{B_\theta}\left[1.66\left(1+\frac{T_i}{T_e}\right)\frac{1}{n_0}\frac{dn_e}{dr} + \frac{0.47}{T_e}\frac{dT_e}{dr} - \frac{0.29}{T_e}\frac{dT_i}{dr}\right] \tag{37}$$

when electron-electron collisions and the energy dependence of the collisions are included. Now the effective density gradient term in the case of the Lorentz colllsion model must be multiplied by a factor 1.66 and expressions (33) and (34) or (35) used for the temperature gradient contributions. Thus, in the first case for example, we obtain

$$\delta j_{bs} = 2.36 \frac{n_0 T_e}{B_\theta} \left(1 + \frac{T_i}{T_e}\right) \frac{1}{n_0} \frac{d n_0 \gamma}{dr} I \tag{38}$$

where we note $I = -\sqrt{(2r/R)}c$, with the constant c depending on the function $h(\theta)$ describing the poloidal variation of the plasma density.

4.9. Conclusions

We have investigated the effect of poloidal variations of the plasma density, $\delta n = \gamma h(\theta) n_0$, on the bootstrap current in a large aspect ratio tokamak equilibrium, such as might arise in gas-puffing experiments, recycling neutral influxes or as a result of toroidal rotation. The calculation has assumed that the lowest order distribution function is Maxwellian for simplicity, although it may be distorted from a simple Maxwellian in reality. A more realistic distribution function might produce additional effects on the bootstrap current, but it would be much more difficult to obtain this function and calculate the consequences. The effect of the poloidal temperature variations resulting from this density variation has also been addressed, as has the generalisation to an arbitrary axisymmetric toroidal geometry. Three explicit cases for the density variation have been considered: case (a) which is sinusoidal and up-down symmetric and is also relevant to the effect of toroidal rotation; case (b) which is sinusoidal and symmetric in the inboard-outboard direction (the effect of sinusoidal symmetry about any other poloidal angle could be deduced simply from decomposing it into a combination of the cases (a) and (b)), and case (c) which is a very localised poloidal variation, approximated by a δ-function in poloidal angle. In case (b) we find the incremental current vanishes exactly, while for case (c) the results naturally depend on the poloidal angle α, describing the location of the neutral influx. We find that the largest effect in this case does occur for localisations near the inboard side of the plasma column. Whether and by how much the bootstrap current increases or decreases depends on both the magnitude and sign of an integral, I, specific to each poloidal density variation, $h(\theta)$, and the amplitude and sign γ, of this variation.

The result for case (c) also serves as a Green's function for calculating the bootstrap current response to an arbitrary poloidal distribution for the density perturbation numerically by a simple quadrature; it also clearly demonstrates why the current vanishes in case (b), or indeed in any up-down symmetric case. Furthermore, it facilitates the treatment of a general, axisymmetric toroidal geometry, albeit requiring there to be only a small number of trapped particles to justify the use of the simple pitch-angle collision operator. We also limit ourselves to up-down symmetric equilibria to simplify the calculation. Although we employed a Lorentz collision operator, appropriate to electron-ion collisions, we demonstrate that our results can be readily adapted to allow for the effects of electron-electron collisions, energy-dependent collisions and the poloidally varying electron and ion temperature perturbations, $\delta T_{e,i}(\theta)$, that

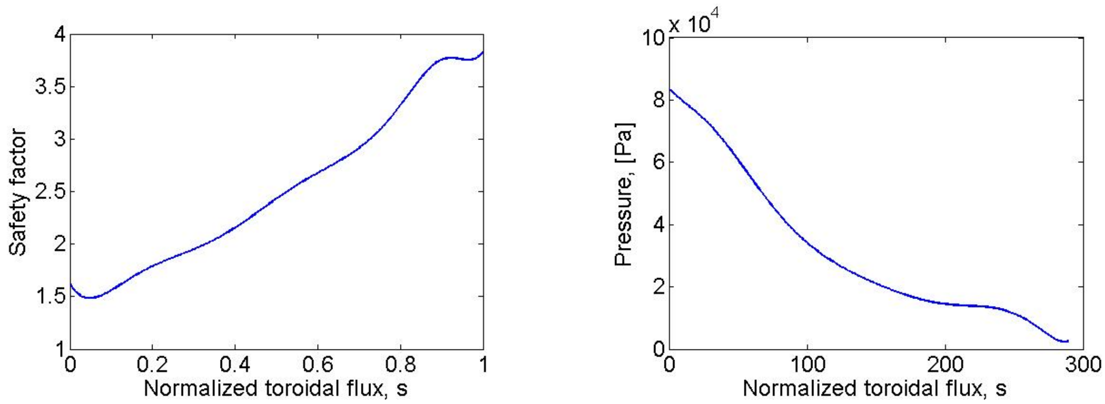

(a) q profile

(b) p profile

Figure 8. Pressure and safety factor profiles for the current driven mode.

would ensure pressure remains constant on a flux surface (and restores the usual poloidally varying Pfirsch-Schluter current as a consequence).

One can expect this poloidal density variation to be linked to the location of any neutral influx or, perhaps, gas-puffing. Thus, an up-down symmetric case may be related to case (a), while symmetric vertical locations near upper and lower X-points may relate to case (b). Case (c) appears to provide a good representation of the results of gas-puffing experiments

The differences in the magnitude and sign of the incremental bootstrap current caused by the nature of the poloidal density variations may have implications for Type 1 ELMs and their control, since their onset is believed to be triggered when peeling-ballooning modes, whose stability is affected by edge plasma currents, become unstable.

5. QH mode

5.1. VMEC equilibrium modelling

Candidate modes which may explain the QH-mode are investigated using the VMEC [40] non-axisymmetric equilibrium code and the linear ballooning stability code COBRAVMEC [41, 42]. Previous work has investigated how such a saturated MHD mode may appear at the plasma edge [15]. It has been shown that such a mode can appear due to the q profile being just below a rational value at the plasma edge. This is the external kink mode, see Fig. 8(a) showing the q profile. VMEC models the plasma as a current carrying plasma column with a vacuum region outside. This allows the q value at the plasma edge to be well defined. In reality these are diverted plasmas and so formally the q will go to infinity at the plasma edge. This would mean that external kink modes are unlikely to form. However, error fields and other non-axisymmetric fields may well create a stochatic layer at the plasma edge so that there is a maximum edge q. An improved understanding of the physics of the separatrix and external kink modes is required.

A saturated MHD mode can also appear as a result of a pressure driven mode and a

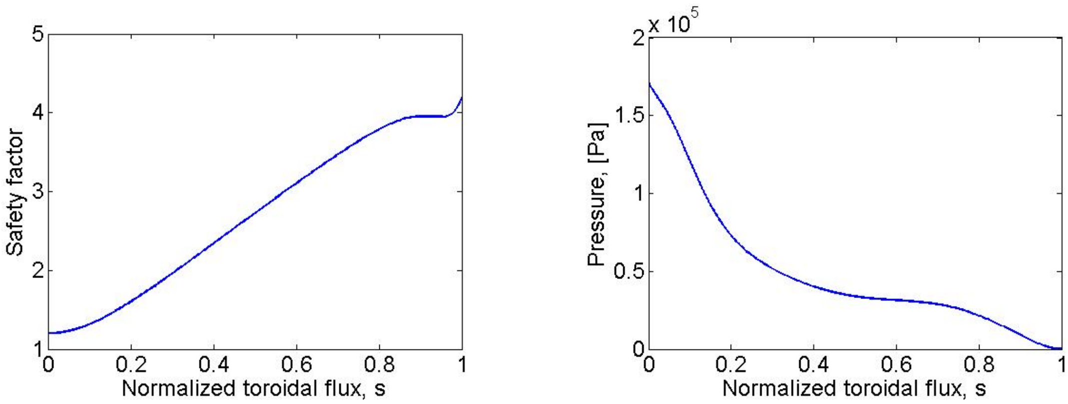

(a) q profile (b) p profile

Figure 9. Pressure and safety factor profiles for the pressure driven mode.

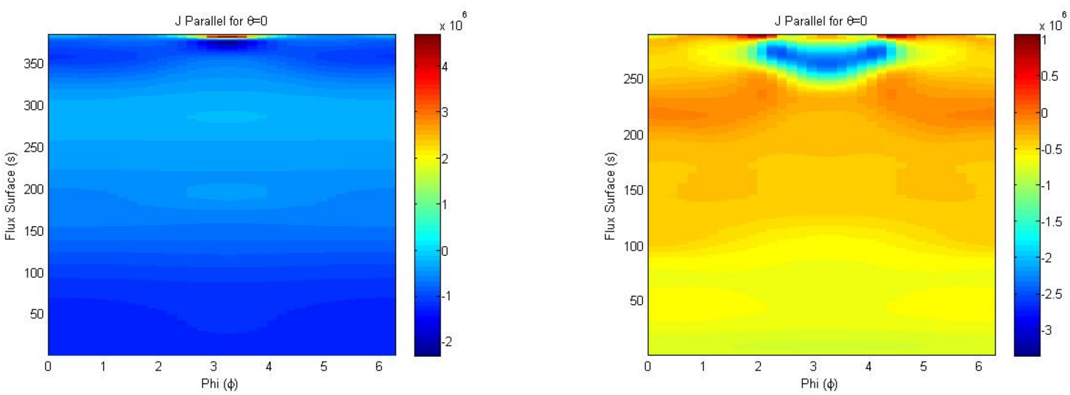

(a) Parallel current for pressure drive mode (b) Parallel current for current drive mode

Figure 10. Parallel current for the current and pressure driven modes. A much broader current ribbon appears for the current driven mode than for the pressure driven mode.

flattening of the q profile which is caused by the bootstrap current, see figure 9(a) showing the q profile for this mode. Note that the q profile is above four at the edge which removes drive for the current driven mode. We call this second type of mode the exfernal mode (after Brunetti [43]). We expect this pressure driven mode to appear at low collisionality as it requires a significant bootstrap current to flatten the q profile at the edge.

We investigate the differences between the external kink mode and the exfernal mode to help to understand which of these modes we see experimentally. It has been noted by Solano et al [13] that in JET a current ribbon appears at the plasma edge. We have processed the external kink mode and exfernal mode equilibria to see if a current ribbon is in evidence. Figure 10 shows the parallel current for the external kink mode and the exfernal mode. We see that the external kink mode has a current ribbon in the pedestal region while the exfernal mode only has a current perturbation at the very edge of the plasma.

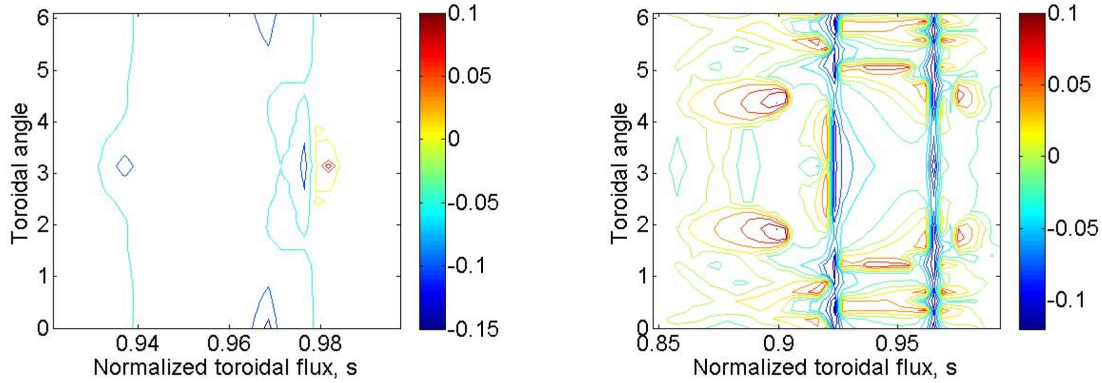

(a) Ballooning mode growth rate for the pressure driven mode

(b) Ballooning mode growth rate for the current driven mode

Figure 11. Linear ballooning mode growth rates for the external kink and pressure driven modes.

5.2. Linear ballooning stability

We now investigate the local linear ballooning stability using the COBRAVMEC code. This calculates the growth rate of the local ballooning mode on a given fieldline. It can also be thought of as the infinite-n ballooning mode. This is of interest because it captures some of the instability drive of the kinetic ballooning mode (KBM). The KBM is thought to drive particle transport, rather than heat transport, which is an important element of the QH-mode [44]. We first calculated ballooning stability for axisymmetric sister equilibria for the cases that are unstable to external kink mode and exfernal mode. Ballooning modes are found to be stable to these axisymmetric equilibria. In contrast, for the 3D equilibria corresponding to the external kink saturated state, strong ballooning instability is found over a large fraction of the edge region, see Fig. 11. The 3D equilibria corresponding to the exfernal mode saturated state is only weakly unstable to ballooning modes, and only very near the edge. Ideal MHD infinite n ballooning instability in the external kinked 3D equilibria could imply ballooning related, or KBM related, density transport

This result may have been expected since it is well known from the physics of resonant magnetic perturbation (RMP) ELM suppression and mitigation that density pump out is only seen when the plasma response is external kink like (i.e. largest around the X-point) rather than ballooning-like [45](where ballooning-like in this context means pressure driven exfernal like). In RMP cases we would not expect to see the current ribbon at the plasma edge as this effectively comes from the coils around the plasma.

5.3. Conclusions

We examined two types of MHD mode which can produce saturated free boundary states: an external kink mode and a pressure driven, exfernal, mode. We have shown that the external kink mode produces a perturbed current ribbon at the plasma edge in line with experimental observations. We have also calculated the linear local ballooning stability of these saturated modes. The external kink mode significantly destabilizes the ballooning modes while the pressure driven mode does not. This result matches expectations from the results of RMP ELM control experiments which show that density pump out only occurs for plasmas with an external kink mode response. The hypothesis is that the KBM produces sufficient partical transport such that the pedestal never reaches the peeling ballooning boundary and so no ELMs occur.

6. Summary and Directions for future work

We have completed various strands of work to improve our understanding of reactor relevant pedestals. While we have some understanding of what sets the pedestal height and width there is still much to understand. We have investigated how to improve the EPED model by trying to remove assumptions about the density. We have tried to determine if a gyrokinetic calculation of the heat flux could help us to determine the density profile. Unfortunately, the linear gyrokinetic results (and probably the nonlinear results too) are not able to discriminate between differing pairs of density and temperature profiles. We believe that this comes from the pedestal transport criterion assumed in EPED. This assumption should be relaxed in future work. It has been observed that density is not a flux surface function in many plasmas due to, for example, plasma rotation or plasma fuelling. We have calculated the effect of non flux surface density on the bootstrap current analytically in this paper and numerical investigations using ELMFIRE have also been completed [9]. This changed bootstrap current will also change the stability of the peeling ballooning modes and thus the ELM stability. We have calculated the effect of non flux surface density using JOREK within the project. This indicated that the low n modes became more unstable and the high n modes were unaffected. This was preliminary work and further confidence in the equilibrium is needed before this can be regarded as a final result. Indeed improving our understanding and measurements of the bootstrap current is still an important topic of research. The effect of plasma turbulence on the bootstrap current is yet to be determined and will require a code such as ELMFIRE to be resolved.

Type I ELMs will not be allowable in reactors due to the damage they will cause to plasma facing components. We will therefore need to develop our confidence in small and no ELM regimes. We investigated the QH-mode using the non-axisymmetric equilibrium code VMEC. In this paper we built on work looking at current and pressure driven modes. Linear ballooning stability analysis indicates that the QH-mode is a saturated external kink mode rather than a pressure driven mode. A gyrokinetic analysis of these equilibria would allow us to understand the effect on transport of non-axisymmetric saturated instabilities. This would also be an important step in understanding RMP ELM control experiments. Work was carried out on other small ELM regimes within this collaboration which will be reported elsewhere. There are lots of avenue for further work including use of the gyro-landau-fluid model implemented in BOUT++ to model I-mode.

A final aspect of this collaboration is the use of neural networks to produce fast surrogate models. This will be important if we hope to use these models to design reactors and to scan large regions of parameter space for favourable reactor relevant conditions.

Acknowledgements

This work resulted from a collaboration under the EUROfusion Enabling Research grant on Reactor Relevant Pedestals (ENR-MFE19.CCFE-04-T002-D001). This work was supported in part by the Swiss National Science Foundation. CJH would like to acknowledge the work of Samuli Saarelma who was the original PI for this project. CJH also wishes to thank B Chapman who was the primary originator of Section 3 and J W Connor who produced Section 4. JWC would like to acknowledge Jim Hastie, Per Helander, Howard Wilson and James Simpson for their thoughts and comments. BC would like to acknowledge Lorenzo Frassinetti for preparation of the JET profile and useful discussions.

This work has been carried out within the framework of the EUROfusion Consortium and has received funding from the Euratom research and training programme 2014-2018 and 2019-2020 under grant agreement No 633053 and from the RCUK [grant number EP/T012250/1]. To obtain further information on the data and models underlying this paper please contact PublicationsManager@ukaea.uk. The views and opinions expressed herein do not necessarily reflect those of the European Commission.

References

[1] C.J. Ham, A. Kirk, S. Pamela, and H. Wilson. Filamentary plasma eruptions and their control on the route to fusion energy. *Nature Reviews Physics*, 2(3):159–167, 2020.

[2] P. B. Snyder *et al* . A first-principles predictive model of the pedestal height and width: development, testing and iter optimization with the eped model. *Nucl. Fusion*, 51:103016, 2011.

[3] S. Saarelma et al. Self-consistent pedestal prediction for JET-ILW in preparation of the DT campaign. *Physics of Plasmas*, 26:072501, 2019.

[4] E Belli and J Candy. Kinetic calculation of neoclassical transport including self-consistent electron and impurity dynamics. *Plasma Phys. Control. Fusion*, 50:095010, 2008.

[5] E Belli and J Candy. Full linearized fokkerplanck collisions in neoclassical transport simulations. *Plasma Phys. Control. Fusion*, 54:015015, 2012.

[6] O. Sauter *et al* . Neoclassical conductivity and bootstrap current formulas for general axisymmetric equilibria and arbitrary collisionality regime. *Physics of Plasmas*, 6:2834, 1999.

[7] R. Hager *et al* . Bootstrap formula. *Physics of Plasmas*, 23:042503, 2016.

[8] J. A. Heikkinen et al. Elmfire. *Journal of Computational Physics*, 227:5582, 2008.

[9] T .Kiviniemi *et al* . Simulating the effect of poloidal particle source on the bootstrap current in tokamak edge pedestal. *Plasma Physics and Controlled Fusion*, in preparation, 2021.

[10] G. Huysmans and O. Czarny. MHD stability in X-point geometry: simulation of ELMs. *Nuclear Fusion*, 47:659, 2007.

[11] A Gillgren and P Strand. PENN for JET. *in preparation*, 2021.

[12] K.H. Burrell et al. Discovery of stationary operation of quiescent h-mode plasmas with net-zero neutral beam injection torque and high energy confinement on DIII-D. *Phys. Plasmas*, 23:056103, 2016.

[13] E.R. Solano et al. Observation of confined current ribbon in JET plasmas. *Phys. Rev. Lett.*, 104:185003, 2010.

[14] W. Suttrop et al. Elm-free stationary h-mode plasmas in the asdex upgrade tokamak. *Plasma Phys. Control. Fusion*, 45:1399, 2003.

[15] A. Kleiner. Non-linear modelling of saturated internal and external MHD instabilities in tokamaks. *PhD Thesis EPFL Switzerland*, 2019.

[16] D. Brunetti. JET QH-mode. *in preparation*, 2021.

[17] D. Brunetti. Type III ELMs. *in preparation*, 2021.

[18] C. Bourdelle, X. Garbet, F. Imbeaux, A. Casati, N. Dubuit, R. Guirlet, and T. Parisot. A new gyrokinetic quasilinear transport model applied to particle transport in tokamak plasmas. *Physics of Plasmas*, 14(11):112501, 2007.

[19] L Horvath et al. Isotope dependence of the type I ELMy H-mode pedestal in JET-ILW hydrogen and deuterium plasmas. *Nuclear Fusion*, 61:046015, 2021.

[20] F. Jenko, W. Dorland, M. Kotschenreuther, and B. N. Rogers. Electron temperature gradient driven turbulence. *Physics of Plasmas*, 7(5):1904–1910, 2000.

[21] T. Görler, X. Lapillonne, S. Brunner, T. Dannert, F. Jenko, F. Merz, and D. Told". The global version of the gyrokinetic turbulence code gene. *Journal of Computational Physics*, 230(18):7053 – 7071, 2011.

[22] J Simpson et al. Using EDGE2D-EIRENE to simulate the effect of impurity seeding and fueling on the upstream electron separatrix temperature. *Nuclear Materials and Energy*, 20:100599, 2019.

[23] L. Frassinetti, M.G. Dunne, U. Sheikh, S. Saarelma, C.M. Roach, E. Stefanikova, C. Maggi, L. Horvath, S. Pamela, E. de la Luna, E. Wolfrum, M. Bernert, P. Blanchard, B. Labit, A. Merle, L. Guimarais, S. Coda, H. Meyer, and J.C. Hillesheim. Role of the pedestal position on the pedestal performance in AUG, JET-ILW and TCV and implications for ITER. *Nuclear Fusion*, 59(7):076038, 2019.

[24] S. Saarelma, L. Frassinetti, P. Bilkova, C. D. Challis, A. Chankin, R. Fridstrm, L. Garzotti, L. Horvath, and C. F. Maggi. Self-consistent pedestal prediction for jet-ilw in preparation of the dt campaign. *Physics of Plasmas*, 26(7):072501, 2019.

[25] M.G. Dunne et al. The role of the density profile in the asdex-upgrade pedestal structure. *Plasma Phys. Control. Fusion*, 59:014017, 2017.

[26] D.R. Hatch, M. Kotschenreuther, S. Mahajan, P. Valanju, and X. Liu. A gyrokinetic perspective on the JET-ILW pedestal. *Nuclear Fusion*, 57(3):036020, 2017.

[27] D.R. Hatch, M. Kotschenreuther, S.M. Mahajan, G. Merlo, A.R. Field, C. Giroud, J.C. Hillesheim, C.F. Maggi, C. Perez von Thun, C.M. Roach, and S. Saarelma and. Direct gyrokinetic comparison of pedestal transport in JET with carbon and ITER-like walls. *Nuclear Fusion*, 59(8):086056, 2019.

[28] T. Luda, C. Angioni, M.G. Dunne, E. Fable, A. Kallenbach, N. Bonanomi, P.A. Schneider, M. Siccinio, G. Tardini, and and. Integrated modeling of ASDEX upgrade plasmas combining core, pedestal and scrape-off layer physics. *Nuclear Fusion*, 60(3):036023, 2020.

[29] D. Moulton, B. Lipschultz, and J. Harrison. X. *EPS Conference*, 44th EPS Conf. on Plasma Physics, Belfast, June 26-30, paper(X):O6.129., 2017.

[30] R.J. Bickerton, J.W. Connor, and J.B. Taylor. *Nature Physical Science*, 229:110, 1971.

[31] J.W. Connor, R.J. Hastie, H.R. Wilson, and R.L. Miller. Magnetohydrodynamic stability of tokamak edge plasmas. *Physics of Plasmas*, 5:2687, 1998.

[32] J.A. Wesson. X. *Nuclear Fusion*, 37(X):571, 1977.

[33] P. Helander, T. Fulop, and M. Lisak. Tokamak current driven by poloidally asymmetric fueling. *Physics of Plasmas*, 13:102506, 2006.

[34] J. Simpson. X. *Private communication*, (X), 2020.

[35] E.R. Solano and R.D.Hazeltine. Effect of asymmetric sources on tokamak neoclassical transport in the plateau regime. *Phys. Fluids B*, 2(9):2113, 1990.

[36] M. N. Rosenbluth, P.H. Rutherford, J. B. Taylor, E. A. Frieman, and L. M. Kovrizhnykh. *Plasma Phys. Controlled Nuclear Fusion Research*, 1:495, 1971.

[37] P. Helander and D.J. Sigmar. Collisional transport in magnetized plasmas. *Cambridge University Press*, (X), 2002.

[38] M. Abramowitz and Stegun. Handbook of mathematical functions. *(New York: National Bureau of Standards, Applied Mathematics)*, page Chapter 19, 1972.

[39] Erdelyi. Higher transcendental functions. *(McGraw-Hill Book Company inc., New York, Vol. II,*, page chapter XIII, 1953.

[40] S. Hirshman and J. C. Whitson. Steepestdescent moment method for threedimensional magnetohydrodynamic equilibria. *Phys. Fluids*, 26:3553, 1983.

[41] R Sanchez et al. COBRA: an optimized code for fast analysis of ideal ballooning stability of three-dimensional magnetic equilibria. *J. Comput. Phys.*, 161:576, 2000.

[42] R Sanchez et al. COBRAVMEC. *Comput. Phys. Commun.*, 135:82, 2001.

[43] D. Brunetti, J.P. Graves, E. Lazzaro, A. Mariani, S. Nowak, W.A. Cooper, and C. Wahlberg. Excitation mechanism of low-n edge harmonic oscillations in edge localized mode-free, high performance, tokamak plasmas. *Phys. Rev. Lett.*, 122:155003, 2019.

[44] M. Kotschenreuther et al. *Nucl. Fusion*, 59:096001, 2019.

[45] Yueqiang Liu, C.J. Ham, A. Kirk, Li Li, A. Loarte, D.A. Ryan, Youwen Sun, W. Suttrop, Xu Yang, and Lina Zhou. ELM control with RMP: plasma response models and the role of edge peeling response. *Plasma Phys. Control. Fusion*, 58(X):114005, 2016.